Journal of Energy Storage 49 (2022) 104147

Contents lists available at ScienceDirect

Journal of Energy Storage

journal homepage: www.elsevier.com/locate/est

Research Papers

Facile synthesis of a binary composite from watermelon rind using response surface methodology for supercapacitor electrode material

Nurizan Omar [a], Ezzat Chan Abdullah [a,*], Arshid Numan [b], Nabisab Mujawar Mubarak [c,*], Mohammad Khalid [b,*], Siti Rahmah Aid [a], Elochukwu Stephen Agudosi [a]

[a] Department of Chemical and Environmental Engineering, Malaysia-Japan International Institute of Technology (MJIIT) Universiti Teknologi Malaysia (UTM), Jalan Sultan Yahya Petra, 54100 Kuala Lumpur, Malaysia

[b] Graphene & Advanced 2D Materials Research Group (GAMRG), School of Engineering and Technology, Sunway University, No. 5, Jalan University, Bandar Sunway, 47500, Subang Jaya, Selangor, Malaysia

[c] Petroleum and Chemical Engineering, Faculty of Engineering, Universiti Teknologi Brunei, Bandar Seri Begawan BE1410, Brunei Darussalam

A B S T R A C T

The electrode material is critical to the performance of a supercapacitor. Therefore, developing a cost-effective and efficient electrode is an essential step toward broader applications for energy storage devices. This paper reports the development of a novel binary composite from watermelon rind (BCWR) as a nitrogen-rich and high stability precursor for a supercapacitor's electrode. BCWR has been successfully synthesized via one-pot self-purging pyrolysis of watermelon rind waste impregnated with nickel ferrite ($NiFe_2O_4$). The effects of process parameters such as pyrolysis temperature, pyrolysis time and biomass to metal oxide ratio were investigated by response surface methodology (RSM). The statistical analysis showed the optimal synthesis condition for BCWR to be 600 °C pyrolysis temperature, 15 min pyrolysis time, and 75:25 ratio of watermelon rind (WR) to $NiFe_2O_4$. Furthermore, the predicted model and experimental results for the specific capacity of BCWR were determined to be 191 Cg^{-1} and 187 Cg^{-1} at 5 mV s^{-1}. With the experimental validation based on structural, chemical and morphological and electrochemical properties determined by X-Ray Diffraction (XRD), Fourier transform infrared (FTIR), X-ray photoelectron spectroscopy (XPS), field emission electron scanning electron microscopy (FESEM), energy dispersive spectroscopy (EDX), cyclic voltammetry (CV), galvanostatic charge discharge (GCD) and electrochemical impedance spectrometry (EIS) we find that watermelon rind biochar (WRB) and BCWR can be considered as a superior alternative for electrode materials for energy storage applications. Two-electrode cells device configuration of BCWR/WRB supercapattery exhibited high power density and energy density of 750.00 W kg^{-1} and 28.33 Wh kg^{-1} respectively at 1 Ag^{-1} current density. Besides, the calculated charge transfer resistance of the BCWR/WRB supercapattery is 42.35 Ohms.

Introduction

Technology has immensely improved the social life of the world's population. Currently, energy storage has been anticipated to expand considerably in the coming years due to the emergence of electronic devices, robots, electric vehicles, drones and so on [1,2]. Supercapacitors, batteries and fuel cells are the majorly classified energy storage devices employed by the principles of storing electrical charges and converting them to chemical energies [3,4,5].All these devices comprise electrolyte, separator, and positive and negative electrodes that contribute to the major cost for the devices. Thus, the development of cost-effective electrodes is highly in exigency. Furthermore, in recent years, researchers have deliberated genuinely on natural resources preservation to improve energy efficiency and consumption [6]. Therefore, transition metal oxides, carbon materials, conducting polymers, and new metal-organic frameworks have been employed as supercapacitors electrodes [7,8,9,10,11,12]. Among all, carbon materials such as carbon foams, nanotubes, graphene and microporous activated carbons have been used as supercapacitor's electrode due to their outstanding performances [13]. However, their complicated production process and high costs limit their industrial usage.

Alternatively, porous biocarbons such as biochars have considerably been opted as supercapacitors' electrode materials due to simple fabrication method, low cost, renewability and abundance [14]. Supercapacitors can be classified into two categories which are electric double- layer capacitor (EDLC) and pseudocapacitor [15]. In pure EDLC, the capacitance is proportional to the specific surface area and pore distribution of porous activated carbons [14]. In addition, there is no issue of electrolyte depletion in the EDLC system, which aided it in good cyclability. However, batteries still have superiority in terms of energy density. In order to overcome this drawback, pseudocapacitive materials such as transition metal oxides (TMOs) and conducting polymers are

* Corresponding authors.
E-mail addresses: ezzatc@utm.my (E.C. Abdullah), mubarak.mujawar@utb.edu.bn, mubarak.yaseen@gmail.com (N.M. Mubarak), khalids@sunway.edu.my (M. Khalid).

https://doi.org/10.1016/j.est.2022.104147
Received 17 October 2021; Received in revised form 12 January 2022; Accepted 30 January 2022
Available online 6 February 2022

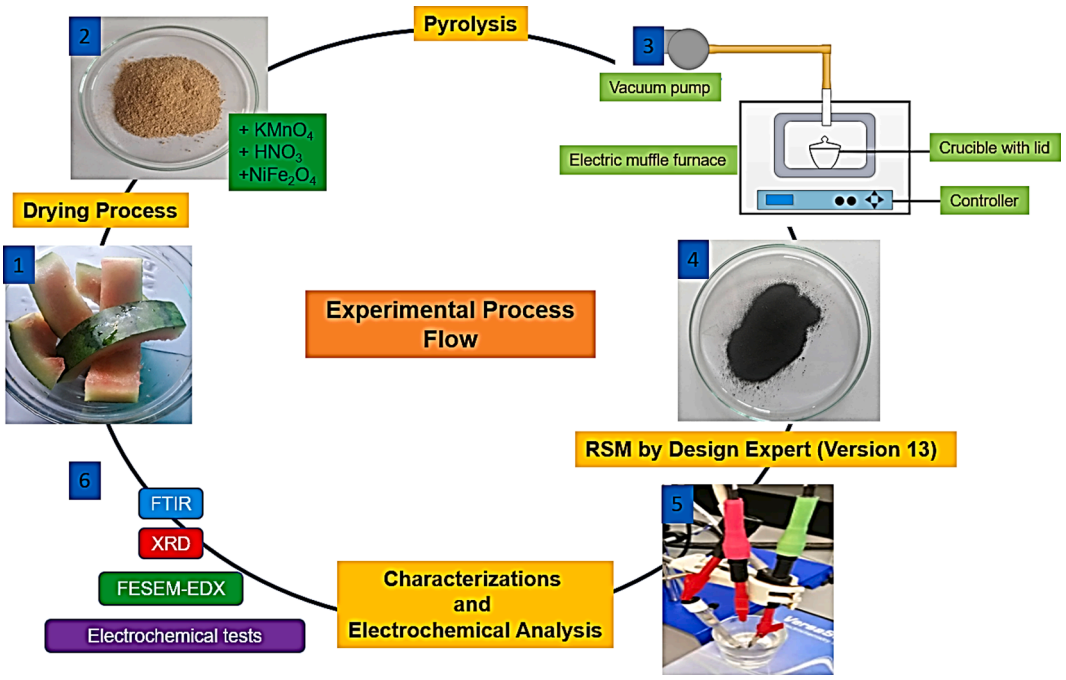

Fig. 1. Schematic flow chart for methodology.

commonly doped with EDLC to upgrade it into a hybrid capacitor in which one electrode exhibits EDLC and another one pseudocapacitor [6,14,16,17].

TMOs are widely used as supercapacitor electrode materials due to their high theoretical specific capacitance, low toxicity, low cost, and good electrochemical activity [18,19]. Furthermore, TMOs are also regarded as ideal pseudocapacitive materials for supercapacitors because they have multiple oxidation states that allow for a wide range of redox potentials. [17,20]. Recent studies have been exploratory about the utilization of TMOs such as NiO_2, Co_3O_4 and MnO_2 which are abundantly available, eco-friendly along with superior redox activity. Besides, the synergistic effects of cobalt and nickel, in particular, have garnered a lot of attention. [18,21]. It's worth noting that cobalt and nickel oxide are both inexpensive to synthesise and have relatively high theoretical capacities, making them the most promising candidates for supercapacitor electrode materials [22,23]. Besides, RuO_2 also has been widely investigated as a promising candidate due to its good conductivity and high specific capacitance. Unfortunately, the cost and rarity of Ru element limit it for bulky application [3,17,24].

Binary metal oxides (BMO) are composed of at least one transition metal ion and one or more electrochemically active/inactive ions, and they can produce more active sites, increase stability, and have synergetic effects of pure oxide. [25]. Furthermore, the idea of making carbon materials with metal oxides, hydroxides or chalcogenides to produce carbon composites may promote superior electrical conductivity from carbon materials with higher storability of dopants which is expected to further enhance the electrochemical performance of the carbon composites [26].

Replacing commercial activated carbon with biochars obtained from agricultural waste is the focus of current research work, which reduces the production cost of supercapacitors and has superfluous environmental considerations. Therefore, watermelon rinds collected from local markets have been used as a biochar production precursor in the present work. Watermelon rind constitutes about 33-35% of watermelon fruit and it is commonly discarded as agricultural food wastes without any treatment, which will constitute solid waste to the environment [27]. In addition, it contains non-essential amino acid citrulline and also carboxyl and amino groups. These compounds contain heteroatoms N and O, which previously reported that by substituting these atoms in the carbon network could significantly improve the specific capacitance of the carbon materials [28,29,30,31]. Incorporating eco-friendly magnetic binary metal oxide, $NiFe_2O_4$ into the biochar production to form magnetic biochar is expected to promote extra charge storage due to faradaic pseudocapacitance from $NiFe_2O_4$. As a result, the electrons are delocalized and migrated within the magnetite structure resulting in high conductivity and enhancing the supercapacitor properties [6,32,33].

This study aimed to develop a binary composite from watermelon rind (BCWR) via self-purging pyrolysis in an electric muffle furnace with limited oxygen conditions. The effects of pyrolysis temperature, pyrolysis time and watermelon rind to binary metal oxide ratio to specific capacity were executed via central composite design (CCD) by Design Expert© (Version 13). The as-synthesized BCWR under the optimum condition and WRB as control sample were-then characterized by XRD, FTIR and FESEM-EDX analysis. Additionally, the electrochemical analysis was conducted to measure the electrochemical performance of fabricated materials in a liquid electrolyte via three-electrodes configuration and two-electrodes device configuration systems.

2. Materials and methods

2.1. Materials

Watermelon rinds were collected from local markets in Kuala Lumpur. First, the flesh residue was removed, then the rinds were cut into small pieces prior to a drying process. The rinds were dried in the oven at 80 ℃ for 24 h, and then an additional drying process at 105 ℃ for another 5 h was required to promote brittleness of the dried watermelon rinds in order to ease the grinding process. The oven-dried watermelon rind was powdered (50–100 μm) using a conventional grinder then stored in an airtight container. Nickel iron oxide ($NiFe_2O_4$), was purchased from Sigma Aldrich, Malaysia. Potassium permanganate ($KMnO_4$), Potassium hydroxide (KOH) and Nitric acid (HNO_3) were supplied by R&M Chemicals, Malaysia. All chemicals and reagents were of analytical grade and were used as received without any further purification. The programmable electric muffle furnace model WiseTherm, FP-03, 1000 °C, 3L was used in magnetic biochar preparation. Nickel foam of uniform thickness (1.6 mm; bulk density of 0.45 g cm^{-3}, porosity of

Table 1
Optimization of process parameters using CCD.

Factor	Independent variables	Ranges and levels		
		Low value (-1)	0	High value (+1)
A	Pyrolysis temperature (C)	600	750	900
B	Pyrolysis time (minutes)	10	35	60
C	WR:BMO ratio (%)	25	50	75

Table 2
CCD for BCWR production.

Run	Point Type	Factor 1A: PyrolysisTemperature (C)	Factor 2B: Pyrolysis Time (Minutes)	Factor 3C: WR: BMO Ratio
1	Factorial	600.00	10.00	25.00
2	Factorial	900.00	10.00	25.00
3	Factorial	600.00	60.00	25.00
4	Factorial	900.00	60.00	25.00
5	Factorial	600.00	10.00	75.00
6	Factorial	900.00	10.00	75.00
7	Factorial	600.00	60.00	75.00
8	Factorial	900.00	60.00	75.00
9	Axial	600.00	35.00	50.00
10	Axial	900.00	35.00	50.00
11	Axial	750.00	10.00	50.00
12	Axial	750.00	60.00	50.00
13	Axial	750.00	35.00	25.00
14	Axial	750.00	35.00	75.00
15	Center	750.00	35.00	50.00
16	Center	750.00	35.00	50.00

95%) was supplied by Sigma–Aldrich, Malaysia. Deionized (DI) water was used throughout the sample's preparations and experiments. The experimental procedures are summarized in Fig. 1.

2.2. Experimental design and statistical analysis

Design Expert© (Version 13) was used in the experimental design and statistical analysis. Central Composite Design (CCD) approach with two levels and three variables was used to determine the relationship between the combinations of experimental parameters with the corresponding response. The three input parameters deployed in the experimental design were the pyrolysis temperature, pyrolysis time and WR: $NiFe_2O_4$ ratio. These parameters were designated as factors A, B and C. All these factors were bound between the lower and upper limit value in which lower coded limits for each factor was -1 while the upper coded limit for each factor was recorded as +1 [34]. The levels of these parameters are represented in Table 1.

The CCD technique was utilized to establish correlation between the experimental parameters (pyrolysis temperature, pyrolysis time and WR: $NiFe_2O_4$ ratio) and the design response (specific capacity (Qs). A total of 16 experiments were conducted based on design layout as expressed in Eq (1). The independent variables and the responses were recorded accordingly in Table 2.

$$N = 2^n + 2n + n_c = 2^3 + 2(3) + 2 = 16 \quad (1)$$

Where n represents the number of factors. 2^n, 2n and n_c denote the total number of factorial points, total number of axial points, and total number of center points, respectively.

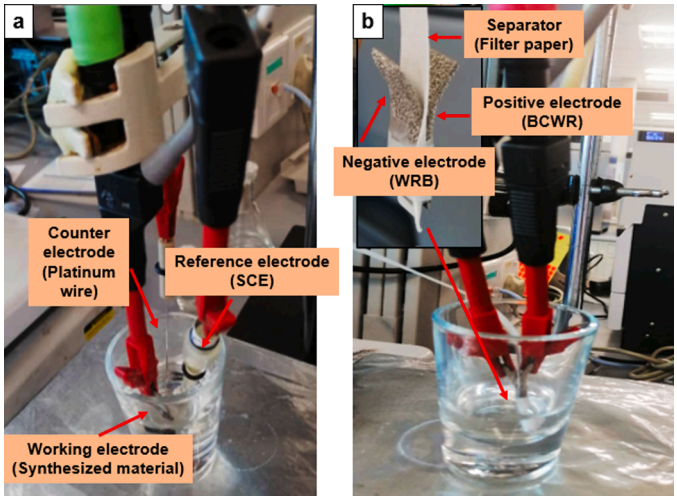

Fig. 2. (a) Three-electrode cells configuration and (b) Two-electrode cells configuration.

2.3. Preparation of biomass precursor and magnetic biochar

A weighted amount of dried watermelon rinds and Nickel iron oxide (according to the specified ratio) were added in the 320 ml solution containing 0.4 M HNO_3 and 0.4 M $KMnO_4$. The mixture was then transferred into a 500 ml Pyrex laboratory beaker before sonochemical treatment using a probe sonicator (brand QSONICA) for 15 min at 70% amplitude. The mixture was then subjected to drying for 48 h at 80 ℃ in the oven to obtain magnetic metal oxide-watermelon rinds precursor. BCWR samples' pyrolysis was performed via an electric muffle furnace (model WiseTherm, FP-03, 1000 °C, 3L) in limited oxygen condition. A closed crucible containing 3 g of $NiFe_2O_4$-watermelon rinds precursor was placed in the middle of the furnace and the furnace's door was closed tightly. Then, the vacuum pump was connected to the syngas effluent's tip at the top of the furnace to suck off the oxygen in order to promote limited oxygen conditions inside the furnace. Next, the samples were pyrolyzed according to the specified time and temperature. The furnace was allowed to cool down upon completion of the pyrolysis before removing the crucible.

2.4. Characterizations

The chemical structure and functional groups in WRB and BCWR were studied using an FTIR (Perkin Elmer Spectrum 1000) fitted with an attenuated total reflectance (ATR) accessory, with the powdered sample put in a diamond crystal gate. FTIR spectra were recorded in the wavenumber range 4000–400 cm^{-1}. The crystalline nature and phase identification of BCWR were recorded by XRD (PANanalytical Empyrean Diffractometer) equipped with Cu K-α radiation (λ = 1.5418 Å) at a scan rate 0.2 s^{-1}, step 0.05° over 2ø, 5° to 90° X-ray photoelectron spectroscopy (XPS) was performed on BCWR using the XPS spectrometer (Thermo Scientific. Waltham, MA, USA) (Thermo Fisher Scientific, England) with Al-Kα X-ray radiation as the X-ray source for excitation from the range of 0 to 1200 eV The surface morphology and elemental composition of the synthesized BCWR were analyzed using FESEM equipped with EDS detector (JEOL: JSM 7800 F).

2.5. Electrode preparation

The working electrodes were prepared by mixing the synthesized BCWR polyvinylidene fluoride (PVDF), and carbon black with a mass percentage ratio of 75:15:10 in 1-methyl-2-pyrrolidone (NMP) medium and stirred for a few hours to obtain a homogenous slurry. The viscous slurry was then dropped and compressed on a 1 cm^2 area of 2 cm X 1 cm nickel foam. The mass loading of BCWR on working electrodes was approximate ~5 mg. The same procedures were applied for WRB and $NiFe_2O_4$ working electrodes.

2.6. Electrochemical analysis

The potentiostat (VersaSTAT 3F) was employed to investigate the

Table 3
ANOVA for BCWR synthesis.

Source	Sum of Squares	df	Mean Square	*F*-value	*p*-value	
Model	159.67	9	17.74	292.61	< 0.0001	significant
A-Temperature	1.30	1	1.30	21.37	0.0036	
B-Time	20.16	1	20.16	332.56	< 0.0001	
C-WR: BMO Ratio	0.9000	1	0.9000	14.84	0.0084	
AB	16.24	1	16.24	267.93	< 0.0001	
AC	34.45	1	34.45	568.10	< 0.0001	
BC	33.62	1	33.62	554.49	< 0.0001	
A^2	0.1717	1	0.1717	2.83	0.1434	
B^2	35.22	1	35.22	580.92	< 0.0001	
C^2	0.0053	1	0.0053	0.0874	0.7775	
Residual	0.3638	6	0.0606			
Lack of Fit	0.3438	5	0.0688	3.44	0.3872	not significant
Pure Error	0.0200	1	0.0200			
Cor Total	160.04	15				

electrochemical competency of the developed electrodes at ambient temperature [35]. KOH (1 M), platinum wire, and saturated calomel electrode (SCE) were used in a three-electrode system as an electrolyte, counter electrode and reference electrode respectively. The electrodes were examined through CV, GCD and EIS. The CV curve was recorded over the specified potential window at 5 mV s^{-1} to 50 mV s^{-1} scan rates and GCD was evaluated at 4 Ag^{-1} to 7 Ag^{-1} current densities. Finally, the impedance measurements were obtained within the frequency range of 0.01 Hz to 100 k Hz at an alternating signal of 10 mV.

2.7. Two-electrode device

For the device development, WRB electrodes (which acts as a negative electrode) are fabricated using Ni-foam and the same ratio of materials (as that of BCWR electrodes). BCWR acts as a positive electrode. Both electrodes are assembled with filter paper in the middle actingas a separator. The measurement systems in three-electrode and two-electrode device configurations are represented in Figs. 2(a) and (b).

3. Results and discussions

3.1. Statistical analysis of BCWR synthesis

The pyrolysis temperature (factor A), pyrolysis time (factor B) and WR: $NiFe_2O_4$ ratio (factor C) as the key process variables were observed in the process optimization. The optimized conditions were determined statistically based on the developed regression model. The regression model equation was developed for the specific capacity of the synthesized BCWR. ANOVA is an important tool that measures the significant differences between means, thereby aiding the understanding of the executed model [36]. In this statistical analysis, the predicted R^2 was 0.9822 and agreed well with an adjusted R^2 of 0.9943. And hence, the recorded R^2 value was 0.9977, which showed that only 0.23% of all the recorded incongruities were not seized by the mode [35]. The high R^2 value confirmed a strong analysis of experimental data in which a good model was predicted as the R^2 value close to unity. Predicted R^2 indicates the accuracy of the response's prediction by the model [37]. The model was significant with an F-value of 292.61 and *p*-value <0.0001. There was only 0.01% chance that a model value of this magnitude could occur due to noise [36]. The low value of Probability >F (*p*-value) and less than 0.05 indicate that the model was very significant. The F-value of lack of fit (3.44) implied that lack of fit was not significant.

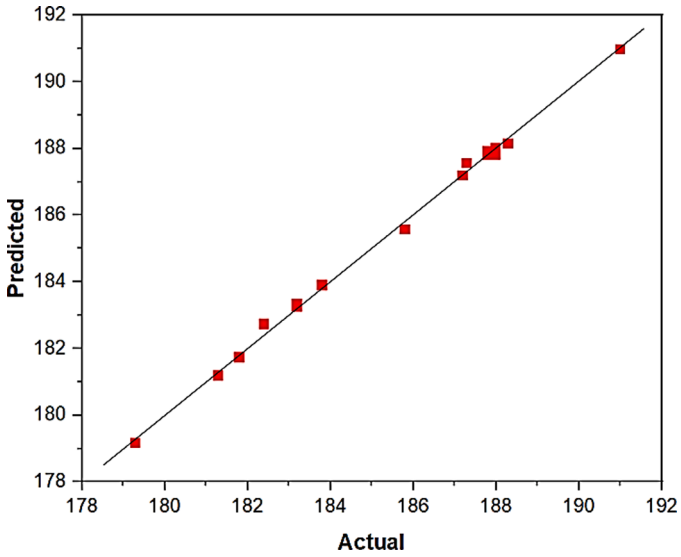

Fig. 3. Relationship between the theoretical values and experimental values of specific capacity, Qs of the synthesized BCWR.

Thus, the significant model terms recorded were B, AB, AC, BC and B^2. The insignificant value of lack of fit implied the model's suitability for synthesizing BCWR as summarized in Table 3.

The quadratic model equation for the specific capacity (Qs) in terms of the coded factors given in Eq. (2). The equation in terms of coded factors can be used to predict the response for a given level of each factor.

$$Q_s = 150.80 - 0.3600A - 1.42B - 0.3000C + 1.42AB - 2.08AC - 2.05BC - 0.2552A^2 - 3.66B^2 + 0.0448C^2 \quad (2)$$

Here, Qs refers to the specific capacity of BCWR while A, B and C are referred to pyrolysis temperature, pyrolysis time and WR: $NiFe_2O_4$ ratio respectively. In Eq. (2), the terms with single factor indicate the individual factor's effect on the response, while those terms that carry two factors indicate the combined effects on the response. The positive sign prior to any terms in the equation represented the synergistic effect, while the negative sign demonstrated the effect of the antagonistic values of those factors [34,35]. Fig. 3 shows the theoretical values against the experimental values of the specific capacity, Qs of BCWR. The results revealed that the predicted values obtained were very close

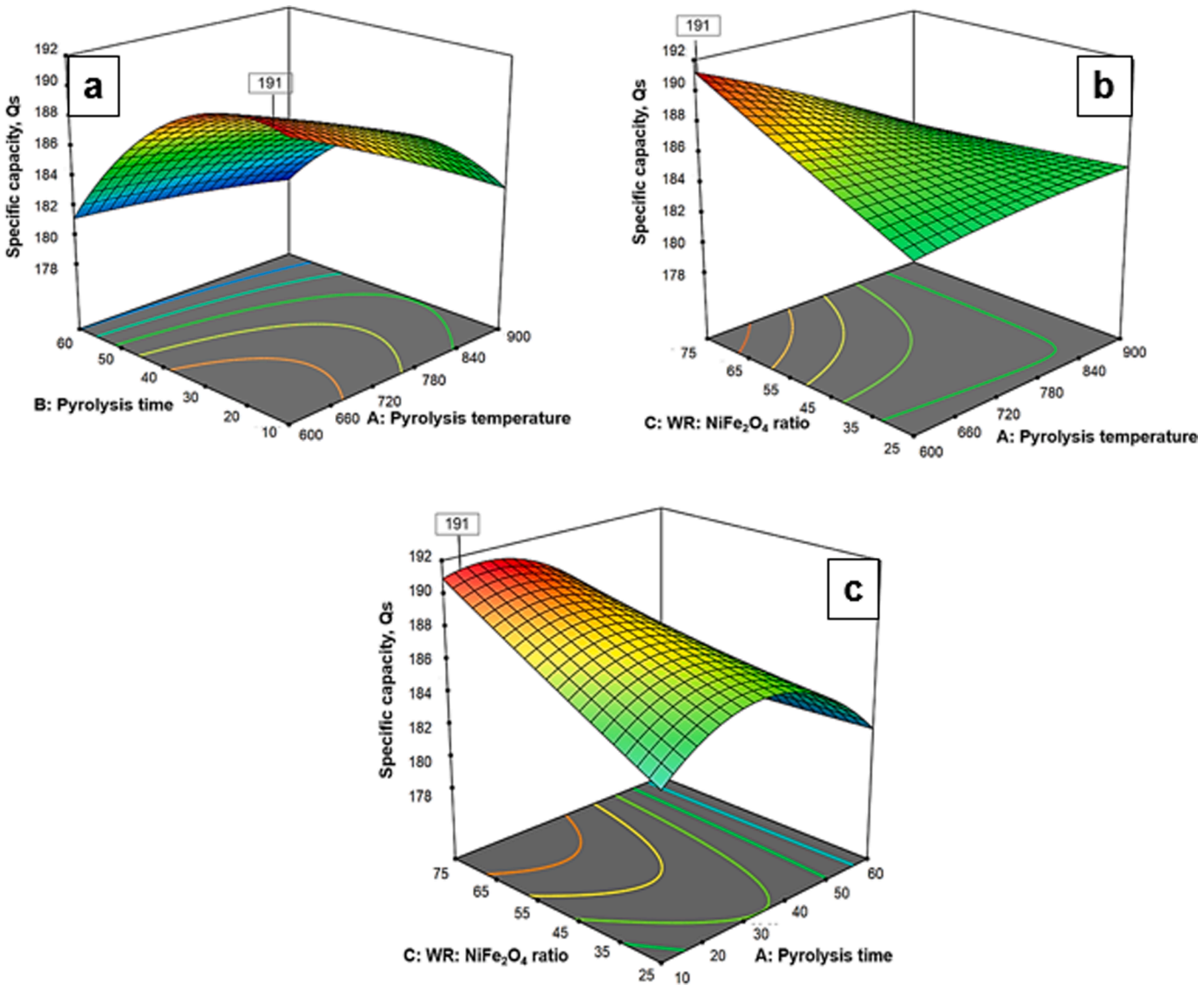

Fig. 4. 3D surface plots for the specific capacity using optimized BCWR synthesis conditions: (a) interactions of pyrolysis time and pyrolysis temperature (b) interactions of WR: NiFe2O4 ratio and pyrolysis temperature, and (c) interactions of WR: NiFe2O4 ratio and pyrolysis time.

to experimental values. Thus, it implies that the model successfully bridged the correlation between the electrode's specific capacity measurement parameters. The highest specific capacity achieved was 191 Cg^{-1}in the 5^{th} run of the experiment while the lowest specific capacity was observed at the 8^{th} run of the experiment with the specific capacity value of 179 Cg^{-1}. An analysis of the studentized residuals of responses confirmed that the selection model accurately estimates the real system. The normal distribution pattern disseminated below and above the straight line reveals that the proposed model is fitted for this study [38, 39].

3.2. Surface analysis of BCWR synthesis

The specific capacity over the various combinations of design factors and their relationships are represented in 3D response surface plots for specific capacity in Fig. 4. Each plot was generated by varying two individual variables while the third variable was kept constant. The specific capacity is minimum at low levels of interactions involving the pyrolysis time and pyrolysis temperature of BCWR as observed in Fig. 4 (a). However, with increasing pyrolysis time, at the lower pyrolysis temperature of 600 ℃, the specific capacity increased and attained the highest specific capacity of 191 Cg^{-1} at 20 min. Further increasing the pyrolysis time, the specific capacity tends to reduce. On the other hand, the specific capacity is maximum at low pyrolysis temperatures and declines as pyrolysis temperatures increase.

Besides, the integrated effect of WR: $NiFe_2O_4$ ratio and pyrolysis temperature for specific capacity of BCWR was demonstrated in Fig. 4 (b). The specific capacity increased as the watermelon rind to binary metal oxide ratio increased from 25 weight percent (wt.%) to 75 wt.%. However, when the pyrolysis temperature increased, there was little difference in the electrode's specific capacity as illustrated in Fig. 4(b). Thus, it elucidated that the maximum specific capacity can be attained when the interactions of both process variables were in the WR: $NiFe_2O_4$ ratio in the range 55–75 wt. % and pyrolysis temperature range of 600–660 ℃. In addition, the response surface plot in Fig. 4(c) describes the effects of WR: $NiFe_2O_4$ ratio with pyrolysis time to the electrode's specific capacity. The results show that WR: $NiFe_2O_4$ ratio has a significant impact on the BCWR electrode's specific capacity. It was attributed to the surface properties and active sites in BCWR which facilitates the ion movements within the electrode and electrolyte interfaces which remarkably enhance the electrochemical properties of the carbon materials [40].

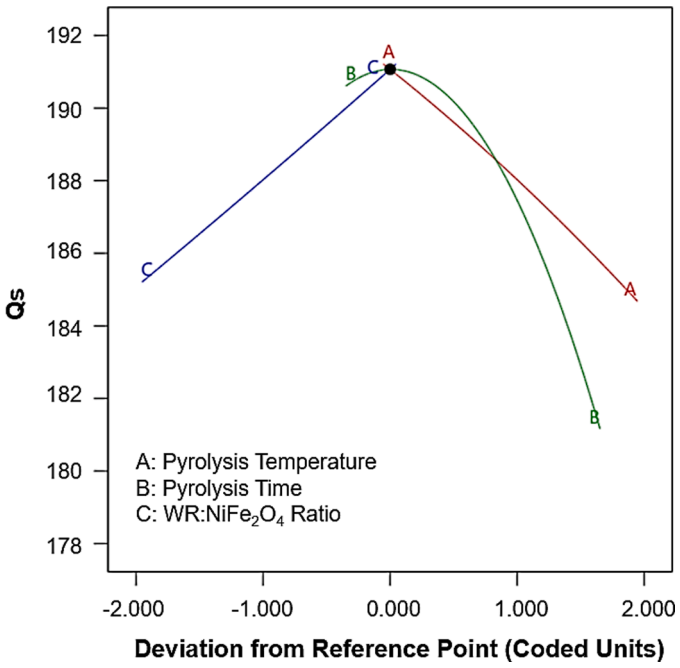

Fig. 5. Effect of perturbation for each process variables in BCWR synthesis.

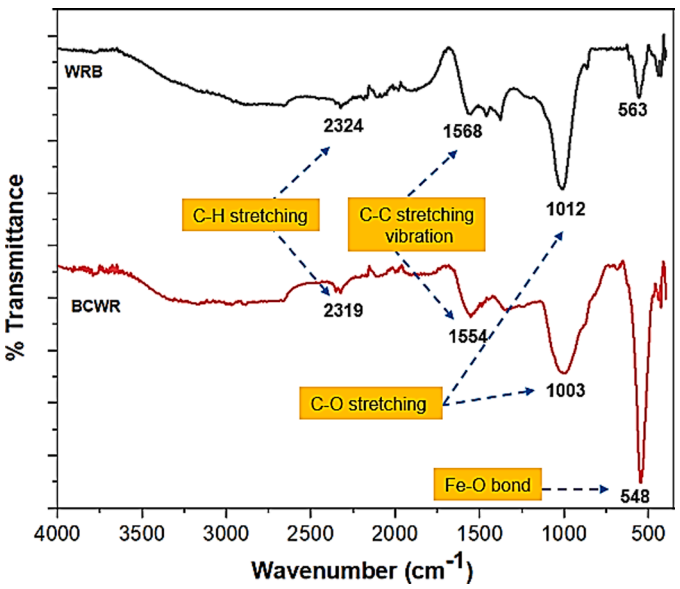

Fig. 6. FTIR spectrum of WRB and BCWR.

3.3. Perturbation effects on specific capacity

Process factors such as pyrolysis temperature, pyrolysis time and WR: $NiFe_2O_4$ ratio influenced the specific capacity of the synthesized BCWR. One important plot in analyzing the level of significance is the perturbation plot, as depicted in Fig. 5. All three factors were plotted on one response graph to generate the perturbation plots. The response graph is plotted with one factor being varied within its window while keeping all other factor positions constant. The response (specific capacity) was plotted over the deviations from the reference point with the synergetic effects of all other factors within its range [35].

The perturbation plot shows that the slopes for factors C and A are in a straight line indicating low significant factors for the process [41,42]. In contrast, a curved line for factor B has been observed, showing the significant effect of the pyrolysis time on the specific capacity of the

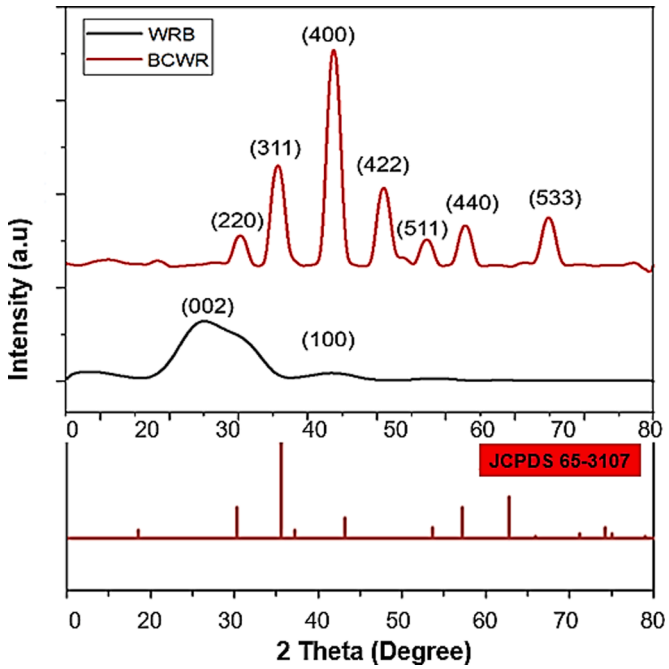

Fig. 7. XRD patterns of WRB and BCWR.

synthesized BCWR. For example, the perturbation of pyrolysis time has both increased and decreased in specific capacity values. If the pyrolysis time is lowered from 20 minutes, it will decrease the specific capacity. A similar effect is also observed when the pyrolysis time increases above 20 minutes.

3.4. Optimization of BCWR synthesis and model validation

The developed model was validated by performing additional experiments based on suggested solutions from the Design Expert © (Version 13). The model predicted optimized values were 191 Cg^{-1}, 600 ℃, 20 min and 75:25 for specific capacity, pyrolysis temperature, pyrolysis time and WR: $NiFe_2O_4$ ratio respectively. After performing additional experiments, a reasonable difference of 4 Cg^{-1} was attained between the experimental data and predicted data from the model. Hence, the predicted model and experimental results for the specific capacity obtained to validate the model were 191 Cg^{-1} and 187 Cg^{-1}, respectively which is only a 0.5% difference obtained from the experimental results; the model is well fitted.

3.5. Chemical structure and functional group analysis

FTIR analysis of WRB and BCWR is shown in Fig. 6. The FTIR results revealed that both WRB and BCWR have almost identical spectra but are different in peak intensity. A broad band was observed around 3600 cm^{-1} for both WRB and BCWR, indicating the adsorbed water and the presence of moisture in the samples [43]. The small peaks around 2000–2400 cm^{-1} in both WRB and BCWR spectrum attributed to the nitrogenous group formation when the biomass was heated at a high temperature which indicated that there was a reduction in the functional groups containing hydrogen and oxygen due to the dehydration and decarboxylation reactions at the high-temperature pyrolysis [44,45].

FTIR spectra around 1500–1600 cm^{-1} represent the C-H bending vibration [46]. The small peak at wavenumber 1453 cm^{-1} at WRB spectrum prescribed the C-O functional group [47]. However, the peak was disappeared for the BCWR sample. The short peak around 1400 cm^{-1} in the BCWR spectrum refers to the C–H in plane bending vibrations in methyl and methylene groups [48]. The sharp peak around 1012 cm^{-1} and broad peak around 1003 cm-1 at WRB and BCWR

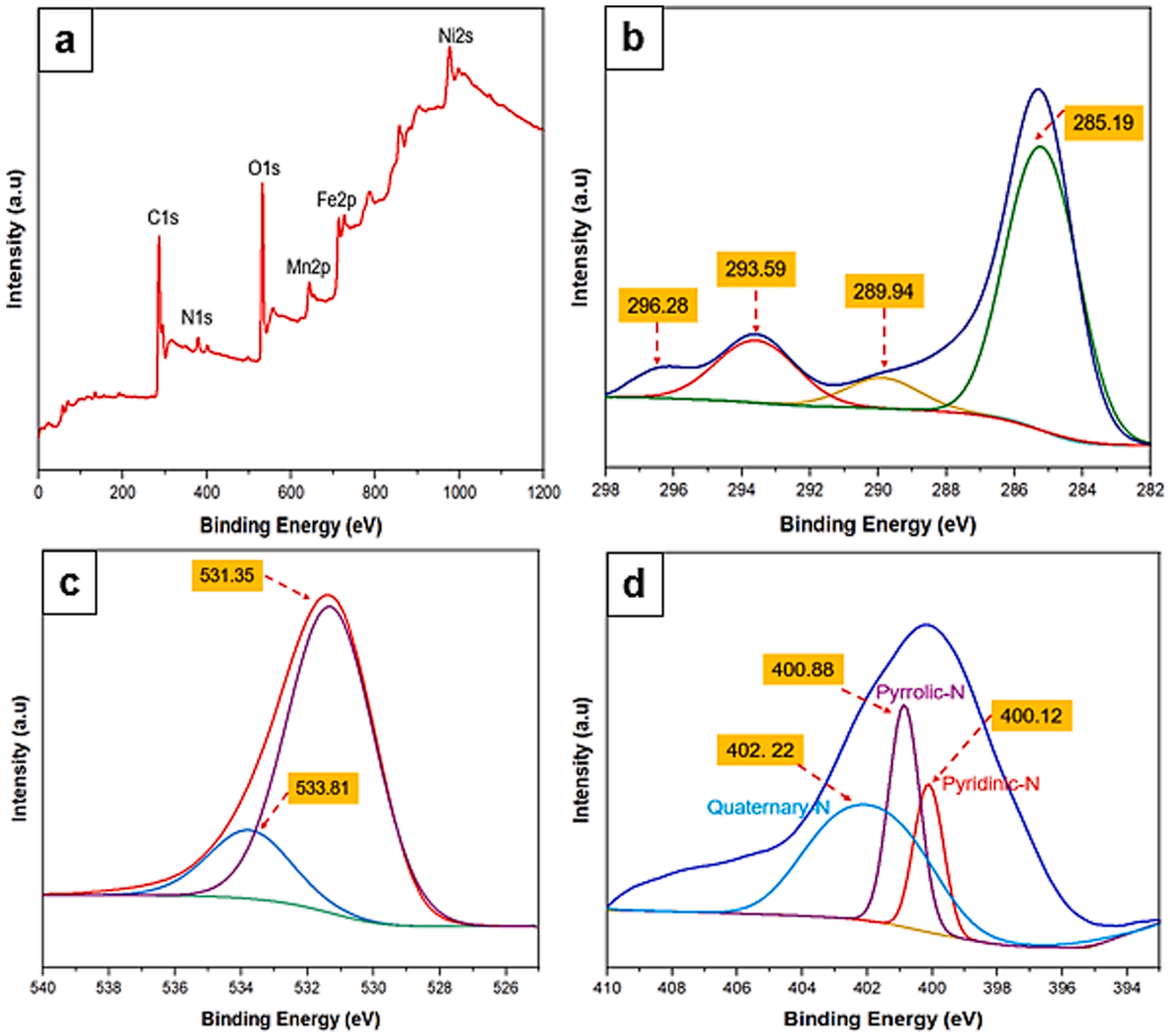

Fig. 8. (a) XPS survey spectrum and High-resolution XPS spectrum of (b) C 1s peaks (c) O 1s peaks and (d) N 1s peaks.

spectrum respectively correspond to the C-O stretching of alcohol and ester groups [49]. The increasing peak intensity at 548 cm^{-1} for BCWR confirms the formation of Fe–O bond which attributes the presence of iron oxides from nickel-iron oxide used in the preparation of the sample for its magnetic properties [50,51]

3.6. Phase analysis

XRD determines the crystallographic structure of WRB and BCWR. XRD patterns were obtained over 2Θ range from 5° to 80° with monochromatized Cu K-α radiation. Fig. 7 provides the XRD patterns of WRB and BCWR. In the XRD profile of WRB, there is evidence of a broad diffraction pattern in with no identifiable features that indicate the crystalline nature of WRB [52]. Thus, WRB's amorphous nature can be postulated [53]. The XRD signature peak at 25° was ascribed to the reflection from (002), indicating that it corresponds to crystalline carbon with extended lattice characteristics [52,54,55]. The small peak around 43° with low intensity in the WRB spectrum corresponds to the (100) crystal plane of carbon [56].

For the XRD spectrum of BCWR in Fig. 7, the diffraction peaks at 2Θ =30.3°, 35.7°, 43.6°, 51.1°, 57.1°, 62.9°, and 74.9° are assigned to the (220), (311), (400), (422), (511), (440), and (533) planes, respectively, according to the cubic spinel ferrites database standard card (JCPDS no. 65-3107) which reveals that the biochar materials were successfully coated with $NiFe_2O_4$ nanoparticles without any other impurities [57,58, 59].

3.7. XPS analysis

XPS analysis was carried out to identify and estimate the nature of the elements present in BCWR sample. The XPS survey spectra in Fig. 8 (a) reveal the presence of C, O, N, Fe, Ni, and Mn as the main elements of the prepared BCWR. Fig. 8(a) depicts the survey spectra confirming the BCWR contain abundant carbon, oxygen and little nitrogen [60]. The N 1s, C 1s and O 1s lines are scanned at higher magnification and deconvoluted, fitted based on the well-known Gaussian fitting method as depicted in Fig. 8(b-d). Moreover, the high-resolution C1s XPS spectrum can be fitted into four individual peaks, which are C-C, C-O and C=O and O-C=O at 285.19 eV, 289.94 eV, 293.59 eV and 296.28 eV, respectively, as demonstrated in Fig. 8(b) [60,61]. The O 1s spectrum in Fig. 8(c) has two characteristic peaks at 533.81 eV and 531.35 eV corresponding to C-O and C=O respectively [61]. The presence of four different N configurations is revealed by the high-resolution XPS spectra of N 1s in Fig. 8(d). The peaks at 400.12, 400.88, and 402.22 eV represent the N

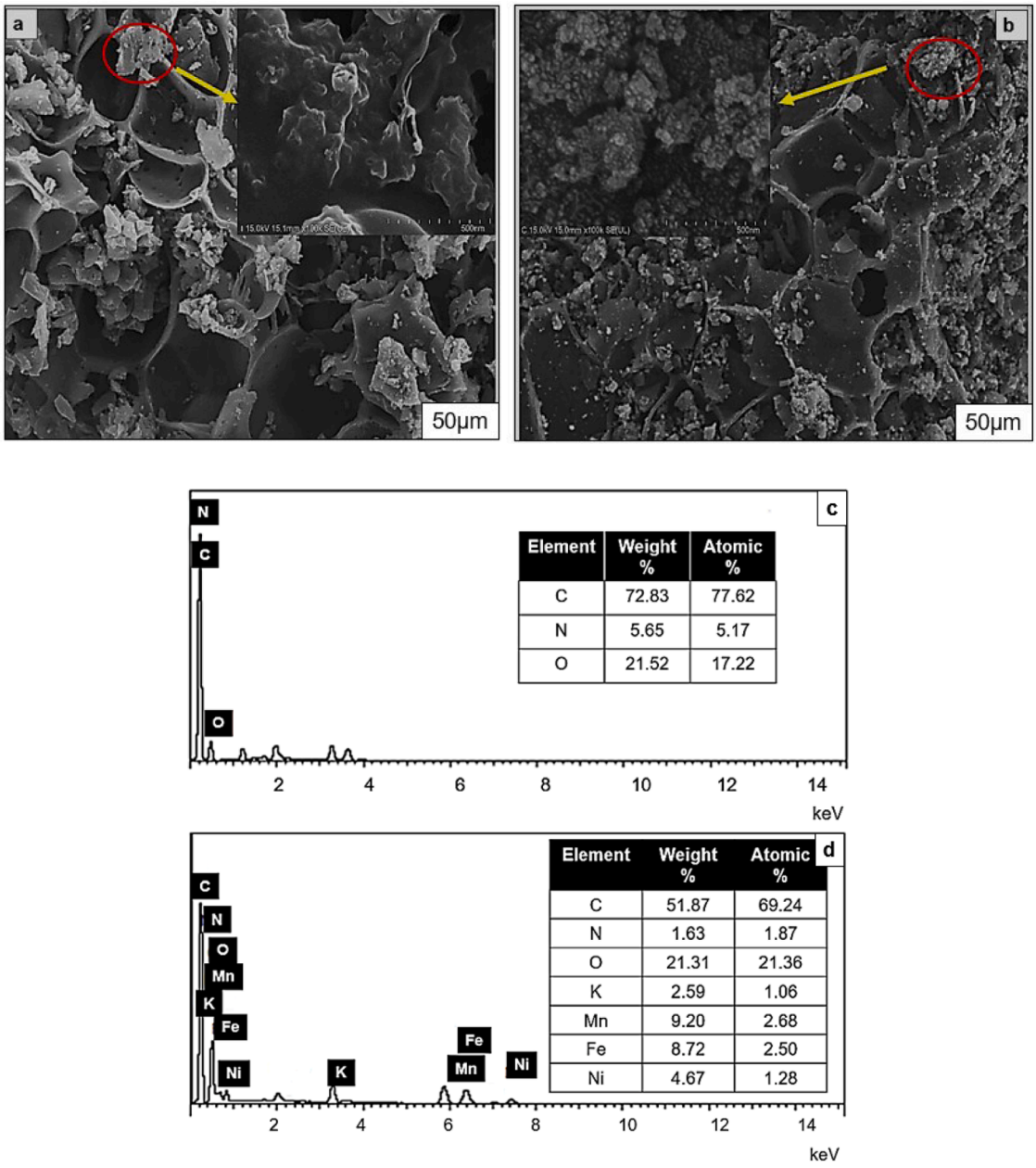

Fig. 9. FESEM images of (a) WRB, (b) BCWR and EDS spectrum of (c) WRB (d) BCWR.

doping in the form of pyridinic-N, pyrrolic-N, and quaternary-N, respectively [62,63,64]. The electrochemical performance of carbons can be improved further by surface functions of O and N due to extra pseudocapacitive behaviour [65].

3.8. Morphological and EDX analysis of WRB and BCWR

FESEM images of WRB and BCWR produced are demonstrated in Fig. 9(a and b). An uneven and heterogeneous surface morphology with a well-developed porous structure on the smooth surface is depicted from the FESEM image of WRB in Fig. 9(a) [48,56]. The pores are generated when small molecules in the watermelon rind are volatilized and depleted during the pyrolysis process [14,66]. BCWR showed high porosity with varied irregular pore sizes following $KMnO_4$ + HNO_3 activation and $NiFe_2O_4$ impregnation, as shown in Fig. 9(b). By improving the porosity channels and introducing functional groups, acid and alkaline treatment could boost the degree of graphitization of biochar [56,67]. Besides, slight agglomerations could be observed in Fig. 9 (b), which could be related to the extraction of some materials, such as dissolution of lignin and other components from the watermelon rind during impregnation, and the escape of the developed volatile compounds from within the particle gradually increased when the final temperature increased during the pyrolysis process [44, 68]. A further EDX elementary composition analysis, as shown in 9(c and d), confirmed the presence of Fe, Ni and O ions in the BCWR sample.

3.9. Cyclic voltammetry analysis

Biomass carbons including biochars contain many oxygen and oxygen-containing groups. Oxygen by negative charge absorbs Fe^{+3} and Ni^{+2} cations and $NiFe_2O_4$ is formed on the biochar surface. It is important to note that by converting biomass to biochar, we have a hydrophobic and conductive biochar-based compound. The proposed electrochemical mechanism BCWR is suggested as in Fig. 10.

The electrochemical performance of WRB and BCWR and $NiFe_2O_4$ was evaluated using cyclic voltammetry (CV), galvanostatic charge

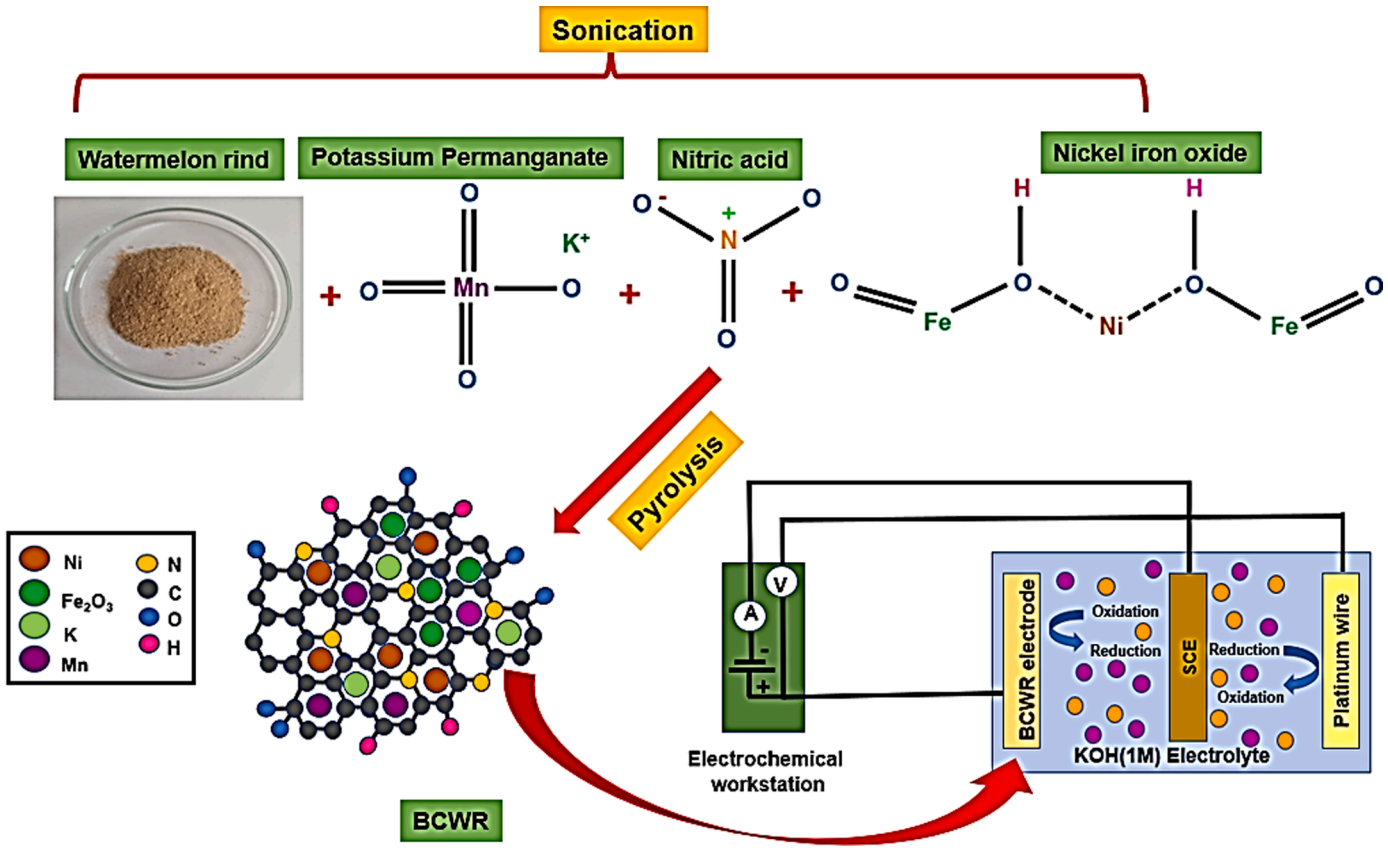

Fig. 10. The proposed electrochemical mechanism for the production of BCWR.

discharge (GCD), and electrochemical impedance spectroscopy (EIS) analysis as presented in Fig. 11(a-h). The CV responses samples at different scan rates (5–50 mV s^{-1}) over the potential window −1–0 V for WRB, while 0–0.5 V for BCWR and $NiFe_2O_4$ in a standard three-electrode cell are presented in Fig. 11(a-c). From Fig. 11(a), the CV curve of WRB shows well defined quasi rectangular shape indicating the behavior of electric double layer capacitor (EDLC) [69,70,71]. While, the CV curve in Fig. 11(b and c) demonstrates well-defined redox peaks indicating the behavior of battery-grade material. The generated symmetric redox peaks can be ascribed to the migration and diffusion of ionic species as the electrolyte is dispersed suggesting that $NiFe_2O_4$ is unveiling battery-type characteristics [35,72].

The samples have higher specific capacity at a lower scan rate as represented in Table 4 since the hydroxyl ions had sufficient time to be migrated in the electrode at a low scan rate which gave higher specific capacity whereas, at a high scan rate, electrolyte ions had less time to diffuse and intercalate into the electrode resulting in a lower specific capacity for WRB, BCWR as well as $NiFe_2O_4$ [6,73]. In addition, it could be observed that an increase in the CV scan rate increases the redox peak current of the electrode, indicating high rate capability and better reversibility behavior [15,74]. The electrochemical performance of the BCWR electrode was greatly enhanced compared to the WRB electrode due to the presence of $NiFe_2O_4$ which enhanced the redox peak current contributing to a significant increase in the electrode performance with better reversibility characteristics.

The high background current for the BCWR electrode compared to the WRB electrode results from the highly conductive binary metal oxide in the BCWR. Therefore, the combination of binary metal oxide into biochar improved the material conductivity, rate capability, reversibility, and cyclic stability [75,76,77,78]. The value of the specific capacity of BCWR electrode prepared at the optimum conditions was measured to be 160 Cg^{-1}. In comparison, the WRB electrode delivered 118 Cg^{-1} under the same optimal conditions by using Eq. (3).

$$Qs = \frac{1}{v \times m} \int_{vi}^{vf} I \times (V) dV \tag{3}$$

where v, V, I, and m are the scan rate, operating potential, current, and mass of active materials, respectively. The integral term represents the region under the oxidation-reduction peaks.

The specific capacity of BCWR in this work is compatible with various other reported nickel ferrite composites electrodes listed in Table 5.

3.10. Galvanostatic charge-discharge analysis

Fig. 11 (c-d) represents GCD plots for WRB and BCWR. The shape of GCD curves for WRB is nearly symmetrical, and the isosceles triangle is formed at various current densities. This shows that WRB has an ideal capacitive behavior. The GCD characteristics were determined different current densities over a potential range of 1.0 V and 0.5 V at room temperature for WRB and BCWR, respectively. According to Eq. (4), the BCWR electrode's specific capacity measured from the GCD plot at 4.0 A/g was 136 Cg^{-1} for BCWR, 112 Cg^{-1} for WRB and 40 Cg^{-1} for $NiFe_2O_4$.

$$Qs = \frac{I \times \Delta t}{m} \tag{4}$$

where I, m, and Δt are the discharge current, mass of active materials, and discharge time reported for a complete discharge, respectively.

Similar trends were observed for specific capacity measurements from GCD as CV measurements. At a lower current density, the electrode's higher charge storage capacity is achieved. Besides, BCWR produces a significant electrochemical performance due to the

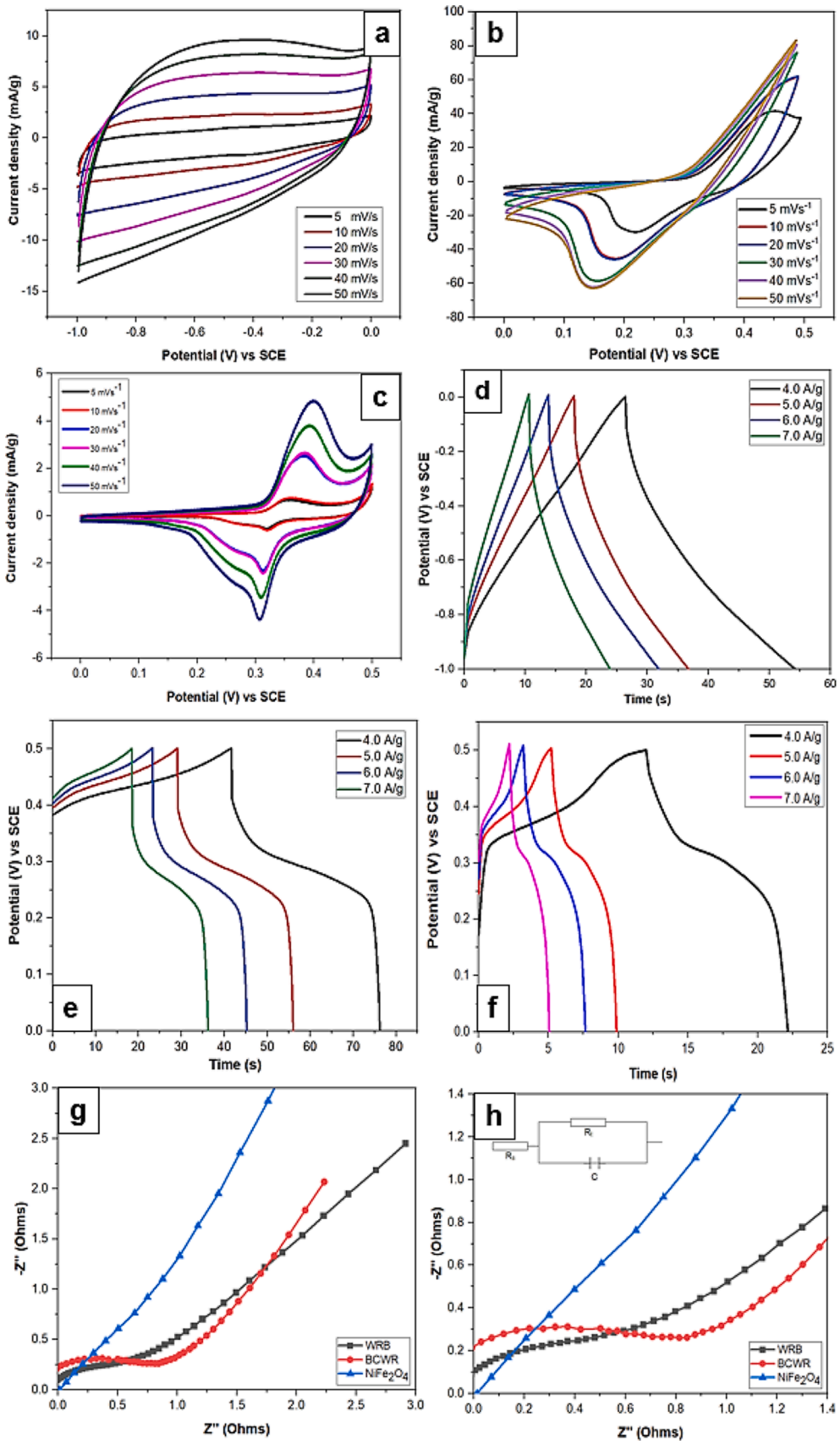

Fig. 11. CV curves of (a) WRB (b) BCWR (c) $NiFe_2O_4$, GCD curves of (d) WRB (e) BCWR (f) $NiFe_2O_4$ and EIS curves of (g) WRB, BCWR and $NiFe_2O_4$, (h) Fitted Nyquist plot of WRB, BCWR and $NiFe_2O_4$ with a corresponding equivalent circuit.

Table 4
Specific capacity of WRB and BCWR at different scan rates.

Scan rate(mVs^{-1})	Specific Capacity(Cg^{-1})		
	WRB	BCWR	$NiFe_2O_4$
5	118.00	187.00	43.00
10	91.00	148.00	41.00
20	76.00	112.00	25.90
30	58.00	73.00	25.10
40	36.00	42.00	21.40
50	29.00	33.00	19.90

conductive platform provided by a combination of biochar as well as the synergistic effect of binary metal oxide. The linear nature of the relationship between the specific capacity and surface area could be seen as demonstrated in the related studies that utilized such materials as NiO, Fe_2O_4 and carbon for energy storage application [6,85,86]. A larger current provides more active sites and environments to generate a larger number of redox reactions due to the electrode material's larger surface area. The redox peaks in CV and GCD curves are indexed to the battery-like behavior and Faradaic reaction of $NiFe_2O_4$. The possible redox reaction is presented in Eq. 5 as follows:

$$Fe^{3+} + Ni^{2+} + 5OH^{-} \grave{a} Fe(OH)_3 + Ni(OH)_2 2Fe(OH)_3 + Ni(OH)_2 \grave{a} NiFe_2O_4 + 4H_2O \quad (5)$$

3.11. Electrochemical impedance spectroscopy analysis

Electrochemical Impedance Spectroscopy (EIS) studies the mechanism of reactant migration and dispersion to and /or away from the electrode surface, which results in a frequency character known as "Warburg impedance"[87]. The slope of the Warburg impedance in the low-frequency region is used to calculate the diffusion resistance since the slope of the line reflects the dynamics of the electrolyte diffusion of the electrode material [88]. Additionally, the impedance of electrode materials can reveal their electrochemical properties. Fig. 11(g) depicts the EIS spectra of $NiFe_2O_4$, WRB and BCWR at the optimum synthesis condition while Fig. 8(h) shows the fitted Nyquist plots with an equivalent circuit.

The impedance plots of WRB and BCWR samples comprise a typical semicircle at the high-frequency region followed by a linear part in the low-frequency region [89]. The nearly 45° line in the middle-frequency region was caused by electrolyte ion diffusion within the electrode pores, whereas the oblique line at the low frequency corresponds to capacitive behavior [90]. A slope of the linear part at a low frequency close to 90° along the imaginary axis -Z″ is known to be a characteristic of an ideally polarizable electrode.

In contrast, a large semicircle at a high frequency indicates high interfacial charge-transfer resistance due to the poor electrical conductivity of electrode materials [91,92]. As shown in Fig. 8, the BCWR sample deviates slightly from the straight line along the -Z″ axis and has a smaller semicircle than the WRB sample, implying good capacitive performance and lower interfacial charge-transfer resistance.

3.12. Two-electrode device fabrication

A supercapattery is a device that combines the characteristics of a capacitor and a battery. In supercapattery, the characteristic parameter is the energy density, which is enhanced by extending the operating voltage window [93]. Due to the fact that energy density is a function of electrode capacity and cell voltage, the supercapattery device incorporating EDLC and battery-grade electrodes makes use of the combined potential window of the two electrodes, resulting in a device with a larger potential window. As schematically depicted in Fig. 12(a), the supercapattery was built using WRB as the negative electrode and BCWR as the positive electrode. Individual cyclic voltammograms for both BCWR and WRB electrodes were done at room temperature as the first stage in the electrochemical research. These preliminary analyses enabled reliable estimates of the highest feasible operating potentials by examining the individual electrode properties. It was observed that BCWR and WRB electrodes operated optimally in the potential range of 0–0.5 V and -1.0–0 V, respectively Fig. 11(a) and 11(b). As seen in Figs. 12(b) and 12(c), the potential window for the constructed BCWR/WRB supercapattery can be increased from 0 to 1.5 V by combining the potential ranges of the BCWR and WRB electrodes. Cyclic voltammograms were recorded at various potential ranges at a fixed scan rate of 10 mV s^{-1} to determine the device's rate capacity, as illustrated in Fig. 12(b). Fig. 12(c) shows the cyclic voltammograms of the completed asymmetric device obtained at various san rates (3–200 mV s^{-1}) over a potential window of 0–1.5 V.

Fig. 12(a) shows that the CV curve was rectangular until a potential of 0.5 V, indicating that charge storage was primarily owing to the EDLC effect. Redox peaks emerged at potentials greater than 0.5 V, indicating that charge storage was due to non-capacitive faradaic processes [94,95,96]. As a result, the charge storage mechanism was due to both EDLC and non-capacitive faradaic reactions spanning the entire potential window of 0 to 1.5 V. Capacitive behaviour contributed to energy storage in the 0–0.5 V potential range, but non-capacitive faradaic redox processes were dominating in the energy storage mechanism beyond 0.5 V. High rate capability and stability of the supercapattery were

Table 5
The various reported nickel ferrite composites electrodes for supercapacitor application.

Material	Method	Electrolyte	Potential range	Specific capacitance (Fg^{-1})	Specific capacity (Cg^{-1})	Scan rate (mVs^{-1})	Ref.
Graphene oxide/$NiFe_2O_4$ composite	Hydrothermal	1M Na_2SO_4	-1.2 and -0.2 V	218.47	218.47	5	[79]
$NiFe_2O_4$/graphene nanocomposite	Solution-based process	1M Na_2SO_4	0 and 1V	207	207	5	[80]
Ternary nitrogen-doped graphene/nickel ferrite/ polyaniline (NGNP)	In-situ polymerization	1M KOH	-0.8 and 0.2 V	645	645	1	[81]
Hybrid of $NiFe_2O_4$/rGO	Hydrothermal	1M KOH	0–0.5 V	584.63	292	10	[82]
$NiFe_2O_4$ /Activated carbon (NFO/AC) composite	$NiFe_2O_4$ was prepared using a facile and cost-effective citrate-gel followed by auto-ignition method	4M KOH	0.25 V–0.65 V	59.52	23.81	10	[83]
Ni-foam/$NiFe_2O_4$ hybrid electrode	$NiFe_2O_4$ nanoparticles are directly grown over the Ni-foam and stainless-steel substrates by a scalable and novel surfactant assisted co-precipitation technique	6M KOH	0–0.5 V	922	461	5	[84]
$NiFe_2O_4$/Watermelon rind biochar or BCWR	Pyrolysis	1M KOH	0–0.5V	374	187	5	This work

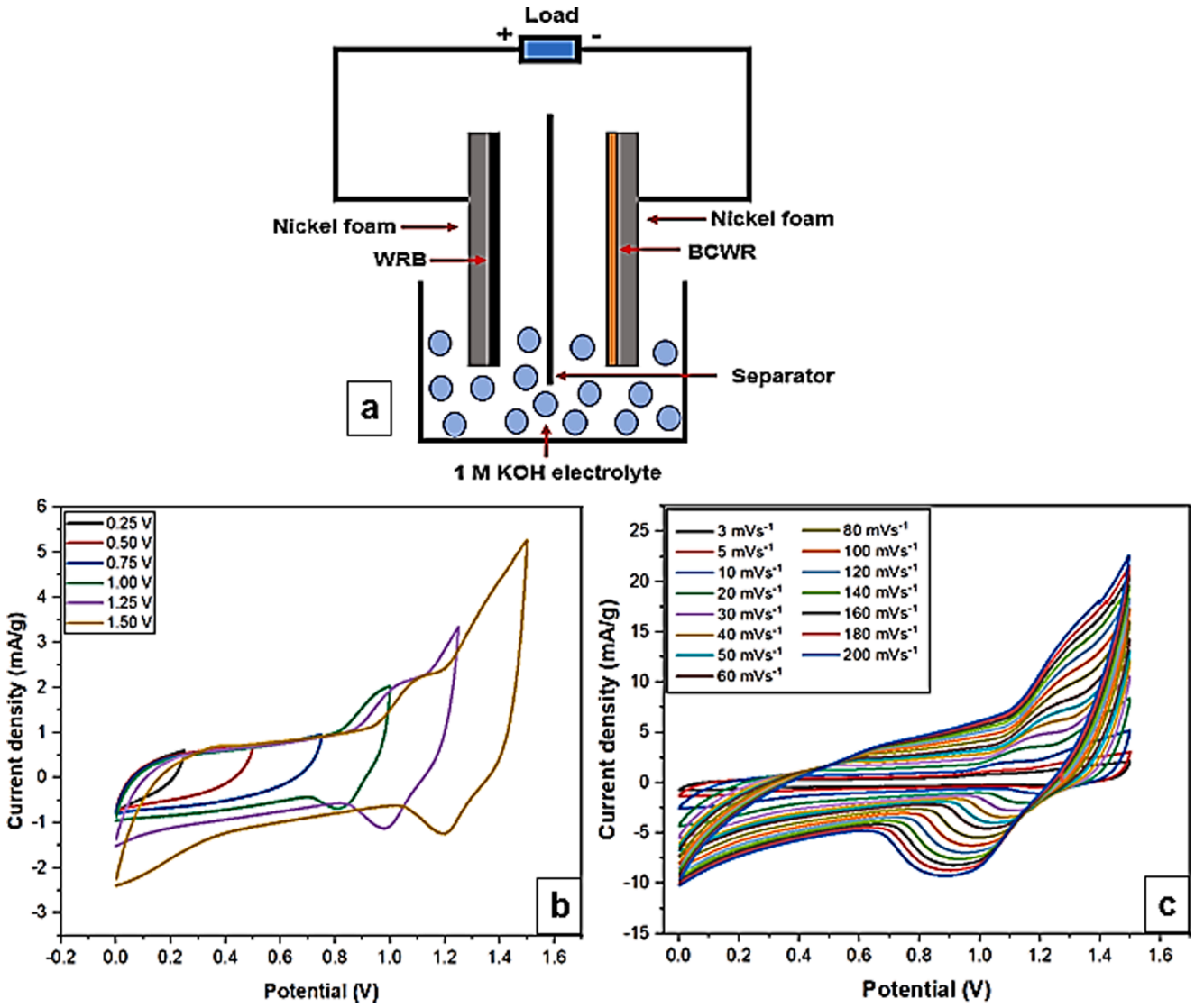

Fig. 12. (a) Schematic illustration of the assembled BCWR/WRB supercapattery (b) CV curve of BCWR/WRB supercapattery measured over different potential windows at a scan rate of 10 mV s^{-1} and (c) CV curve of BCWR/WRB supercapattery measured at diverse scan rates.

demonstrated by the shape, consistency, and amplification of the CV curves at diverse scan rates (3–200 mV s^{-1}).

The specific capacity of the built asymmetric device was calculated using the relationship described in Eqs. (6), (7), and (8), while also taking into account the overall mass loading of the device electrodes. Charge-discharge plots of the BCWR/WRB supercapattery device are shown in Fig. 13(a) over a range of potential windows at the same current density of 4 A/g. While Fig. 13(b) shows charge-discharge plots at a range of current densities in the potential range of 0–1.5 V. The symmetrical charge-discharge plots proved the capacitive nature of the material in conjunction with the strong reversibility of the redox reactions [97]. To determine the efficiency of the built device, the energy density, E (Wh kg^{-1}), and power density, P (W kg^{-1}), of the fabricated supercapattery were measured using the equations specified in Eqs. (7) and (8), respectively [98,99]. Table 6 contains the estimated values of E and P.

$$Qd = \frac{\mathrm{I} \times \Delta t}{3.6\ m} \tag{6}$$

$$E = \frac{\mathrm{Qs} \times \Delta V}{2 \times 3.6} \tag{7}$$

$$P = \frac{E \times 3600}{\Delta \mathrm{t}} \tag{8}$$

where Qd, is the specific capacity of the device (mA h g^{-1}), is the operating voltage window; m, is the total mass of active materials for both electrodes; I, is the discharging current, and Δt is the discharge time.

Fig. 14 depicts the Nyquist plot for the assembled device showing the EIS spectra of the device. As expected, a semicircle was apparent in the high-frequency region whereas, in the low frequency region, a straight line was observed for the device.

The semicircle diameter measurements showed low cell resistance, demonstrating the short path travelled by ions/electrons [100,101]. At the low-frequency region of the plot showed a straight-line gradient (less steep slope) in the Nyquist plot indicating low interfacial diffusion resistance (fast ion diffusion and mass transport at electrode/electrolyte interface) [102,103,104]. Accordingly, the Nyquist plots reported the charge transfer resistances of the device to be 42.35 Ohms.

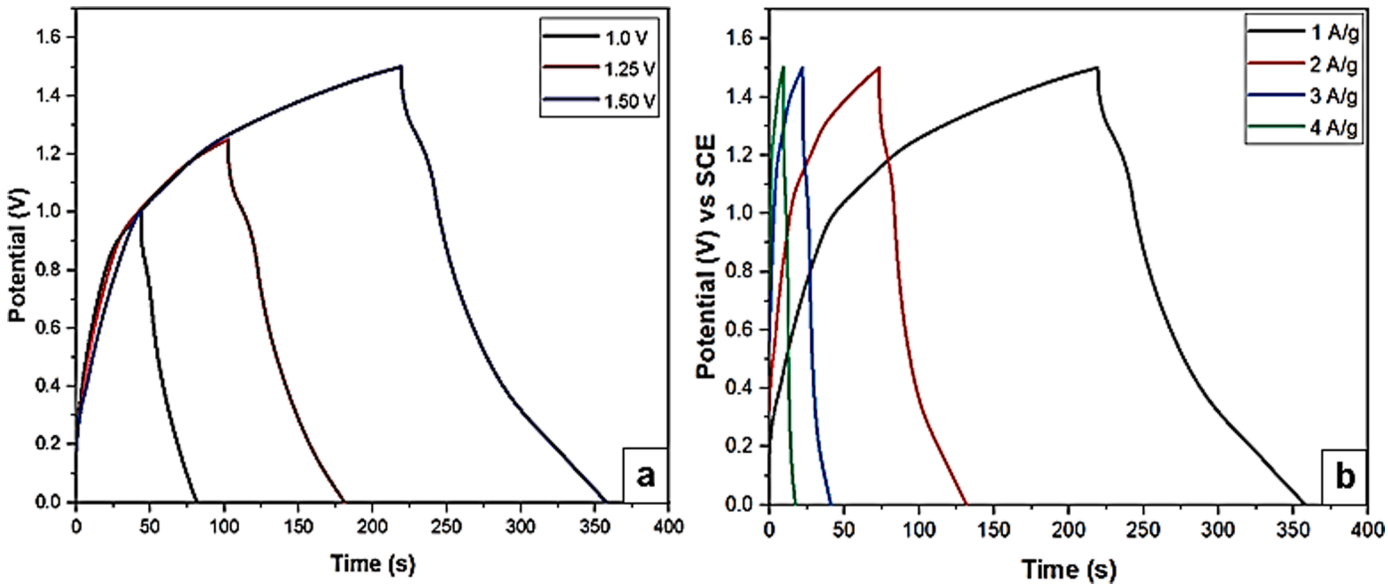

Fig. 13. GCD plots of BCWR/WRB supercapattery measured at (a) different potential windows, and (b) different current densities.

Table 6
Energy density versus power density.

Device	Current density(Ag $^{-1}$)	Energy density(W h Kg^{-1})	Power density(W Kg^{-1})
BCWR/ WRB	1	28.33	750.00
	2	23.83	1500.31
	3	11.80	2250.00
	4	7.38	3000.00

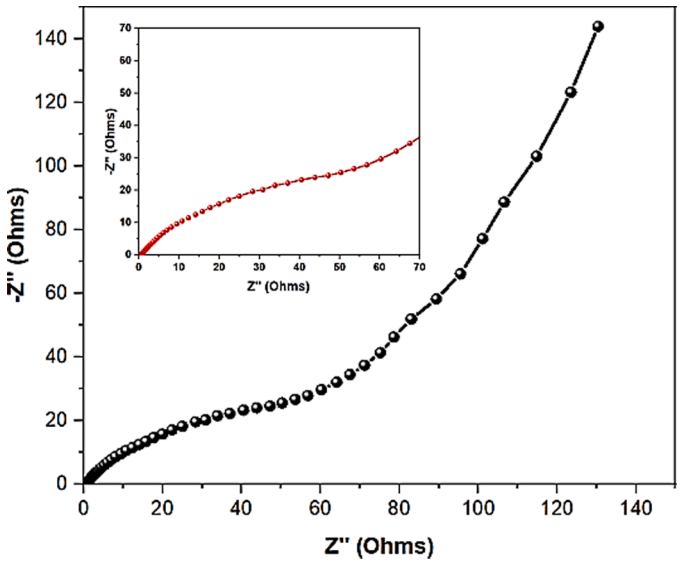

Fig. 14. EIS spectra of the BCWR/WRB supercapattery device.

4. Conclusion

The WRB and BCWR were developed via pyrolysis in a limited oxygen condition electric muffle furnace and investigated for energy storage applications. The statistical analysis revealed that the optimized values for synthesizing BCWR were 600 C, 15 min, and 75:25 for pyrolysis temperature, pyrolysis time and WR to BMO ratio respectively. The FESEM-EDS analyses confirmed the presence of Fe and Ni elements in BCWR. Furthermore, the results of the electrochemical measurements of the developed nanocomposite were 187 Cg^{-1} at 5 mV s^{-1}, 136 Cg^{-1} at 4.0 A/g for BCWR. Two-electrode cells device configuration of BCWR/WRB supercapattery exhibited high power density and energy density of 750.00 W kg^{-1} and 28.33 Wh kg^{-1} respectively at 1 A/g current density. Thus, the results reveal the battery-like features (from CV and GCD) of the fabricated BCWR and its promising potentials to be utilized as electrode material in developing electrochemical energy storage systems.

Author statement

Ezzat Chan Abdullah, Nabisab Mujawar Mubarak and Mohammad Khalid conceived and designed the project. Nurizan Omar performed the experiments, analysed the data, drafted and revised the manuscript. Arshid Numan, Siti Rahmah Aid and Elochukwu Stephen Agudosi contributed in reviewing and editing the manuscript. Ezzat Chan Abdullah, Nabisab Mujawar Mubarak, Mohammad Khalid and Arshid Numan helped to improve the scientific discussion. All authors have read and agreed to the published version of the manuscript.

Declaration of Competing Interest

The authors declare that they have no known competing financial interests or personal relationships that could have appeared to influence the work reported in this paper.

References

[1] Y. Yang, et al., The role of geometric sites in 2D materials for energy storage, Joule 2 (6) (2018) 1075–1094.
[2] K.V.G. Raghavendra, et al., An intuitive review of supercapacitors with recent progress and novel device applications, J. Energy Storage 31 (2020), 101652.
[3] B.L. Vijayan, et al., Thin metal film on porous carbon as a medium for electrochemical energy storage, J. Power Sources 489 (2021), 229522.
[4] J.S. Ko, et al., Differentiating double-layer, psuedocapacitance, and battery-like mechanisms by analyzing impedance measurements in three dimensions, ACS Appl. Mater. Interfaces 12 (12) (2020) 14071–14078.
[5] S. Zheng, et al., Graphene-based materials for high-voltage and high-energy asymmetric supercapacitors, Energy Storage Materials 6 (2017) 70–97.
[6] D. Thomas, et al., Iron oxide loaded biochar/polyaniline nanocomposite: Synthesis, characterization and electrochemical analysis, Inorg. Chem. Commun. 119 (2020), 108097.
[7] W.-H. Li, et al., Conductive metal–organic framework nanowire array electrodes for high-performance solid-state supercapacitors, Adv. Funct. Mater. 27 (27) (2017), 1702067.

[8] F. Wang, et al., Latest advances in supercapacitors: from new electrode materials to novel device designs, Chem. Soc. Rev. 46 (22) (2017) 6816–6854.
[9] H. Wang, et al., Conjugated microporous polycarbazole networks as precursors for nitrogen-enriched microporous carbons for CO2 storage and electrochemical capacitors, Chem. Mater. 29 (11) (2017) 4885–4893.
[10] B. Pal, et al., In situ encapsulation of tin oxide and cobalt oxide composite in porous carbon for high-performance energy storage applications, J. Electroanal. Chem. 817 (2018) 217–225.
[11] D. Liu, et al., Polyaniline coated boron doped biomass derived porous carbon composites for supercapacitor electrode materials, Ind. Eng. Chem. Res. 54 (50) (2015) 12570–12579.
[12] M.T.H. Siddiqui, et al., Synthesis of magnetic carbon nanocomposites by hydrothermal carbonization and pyrolysis, Environ. Chem. Lett. (2018) 16.
[13] Q. Liang, et al., A honeycomb-like porous carbon derived from pomelo peel for use in high-performance supercapacitors, Nanoscale 6 (22) (2014) 13831–13837.
[14] X.-Q. Lin, et al., Self-nitrogen-doped porous biocarbon from watermelon rind: a high-performance supercapacitor electrode and its improved electrochemical performance using redox additive electrolyte, Energy Technol. 7 (3) (2019), 1800628.
[15] X. Dong, et al., Sandwich-like honeycomb Co2SiO4/rGO/honeycomb Co2SiO4 structures with enhanced electrochemical properties for high-performance hybrid supercapacitor, J. Power Sources 492 (2021), 229643.
[16] M.K. Rafiq, et al., Influence of pyrolysis temperature on physico-chemical properties of corn stover (zea mays l.) biochar and feasibility for carbon capture and energy balance, PLoS One 11 (6) (2016), e0156894. -e0156894.
[17] Y. Zhang, et al., Binary metal oxide: advanced energy storage materials in supercapacitors, J. Mater. Chem. A 3 (1) (2015) 43–59.
[18] S. Wang, et al., Morphological control and electrochemical performance of NiCo2O4@NiCo layered double hydroxide as an electrode for supercapacitors, J. Energy Storage 41 (2021), 102862.
[19] Y. Liu, et al., Binary Co–Ni oxide nanoparticle-loaded hierarchical graphitic porous carbon for high-performance supercapacitors, J. Mater. Sci. Technol. 37 (2020) 135–142.
[20] C. Xiang, et al., Simple synthesis of graphene-doped flower-like cobalt–nickel–tungsten–boron oxides with self-oxidation for high-performance supercapacitors, J. Mater. Chem. A 5 (20) (2017) 9907–9916.
[21] S. Fang, et al., Anchoring sea urchin-like cobalt-nickel carbonate hydroxide on 3D carbon sponge for electrochemical energy storage, J. Alloys Compd. 845 (2020), 156024.
[22] P. Wang, et al., Cyanometallic framework-derived hierarchical Co3O4-NiO/graphene foam as high-performance binder-free electrodes for supercapacitors, Chem. Eng. J. 369 (2019) 57–63.
[23] X. Yang, et al., Low-temperature synthesis of sea urchin-like Co-Ni oxide on graphene oxide for supercapacitor electrodes, J. Mater. Sci. Technol. 55 (2020) 223–230.
[24] J. Xie, et al., Layer-by-layer β-Ni(OH)2/graphene nanohybrids for ultraflexible all-solid-state thin-film supercapacitors with high electrochemical performance, Nano Energy 2 (1) (2013) 65–74.
[25] M.V. Reddy, G.V. Subba Rao, B.V.R. Chowdari, Metal oxides and oxysalts as anode materials for Li ion batteries, Chem. Rev. 113 (7) (2013) 5364–5457.
[26] J.F.S. Fernando, et al., Enriched pseudocapacitive lithium storage in electrochemically activated carbonaceous vanadium(iv,v), oxide hydrate, J. Mater. Chem. A 8 (26) (2020) 13183–13196.
[27] R. Thangavel, et al., High-energy green supercapacitor driven by ionic liquid electrolytes as an ultra-high stable next-generation energy storage device, J. Power Sources 383 (2018) 102–109.
[28] J. Liu, et al., Promising nitrogen-rich porous carbons derived from one-step calcium chloride activation of biomass-based waste for high performance supercapacitors, ACS Sustain. Chem. Eng. 4 (1) (2016) 177–187.
[29] B. Li, et al., Nitrogen-doped activated carbon for a high energy hybrid supercapacitor, Energy Environ. Sci. 9 (1) (2016) 102–106.
[30] T. Lin, et al., Nitrogen-doped mesoporous carbon of extraordinary capacitance for electrochemical energy storage, Science 350 (6267) (2015) 1508–1513.
[31] R.-J. Mo, et al., Activated carbon from nitrogen rich watermelon rind for high-performance supercapacitors, RSC Adv. 6 (64) (2016) 59333–59342.
[32] X. Fan, et al., Battery technologies for grid-level large-scale electrical energy storage, Trans. Tianjin University 26 (2) (2020) 92–103.
[33] M.T.H. Siddiqui, et al., Fabrication of advance magnetic carbon nano-materials and their potential applications: A review, J. Environ. Chem. Eng. 7 (1) (2019), 102812.
[34] M. Tripathi, et al., RSM optimization of microwave pyrolysis parameters to produce OPS char with high yield and large BET surface area, Fuel 277 (2020), 118184.
[35] E.S. Agudosi, et al., Optimisation of NiO electrodeposition on 3D graphene electrode for electrochemical energy storage using response surface methodology, J. Electroanal. Chem. 882 (2021), 114992.
[36] A. Kundu, et al., Optimisation of the process variables in production of activated carbon by microwave heating, RSC Advances, 5 (45) (2015) 35899–35908.
[37] M.A. Hossain, et al., Optimization of process parameters for microwave pyrolysis of oil palm fiber (OPF) for hydrogen and biochar production, Energy Convers. Manage. 133 (2017) 349–362.
[38] R. Singh, et al., Biosorption optimization of lead(II), cadmium(II) and copper(II) using response surface methodology and applicability in isotherms and thermodynamics modeling, J. Hazard. Mater. 174 (1) (2010) 623–634.
[39] A.A.H. Saeed, et al., Modeling and optimization of biochar based adsorbent derived from Kenaf using response surface methodology on adsorption of Cd2+, Water 13 (7) (2021) 999.
[40] Y. Liu, et al., Design and preparation of biomass-derived carbon materials for supercapacitors: A review, C 4 (4) (2018) 53.
[41] S. Nizamuddin, et al., Chemical, dielectric and structural characterization of optimized hydrochar produced from hydrothermal carbonization of palm shell, Fuel 163 (2016) 88–97.
[42] B.S. Gupta, J.E. Ako, Application of guar gum as a flocculant aid in food processing and potable water treatment, Eur. Food Res. Technol. 221 (6) (2005) 746–751.
[43] H. Liu, et al., Effect of modified coconut shell biochar on availability of heavy metals and biochemical characteristics of soil in multiple heavy metals contaminated soil, Sci. Total Environ. 645 (2018) 702–709.
[44] M. Noraini, et al., Single-route synthesis of magnetic biochar from sugarcane bagasse by microwave-assisted pyrolysis, Mater. Lett. 184 (2016) 315–319.
[45] A. Mukherjee, A.R. Zimmerman, W. Harris, Surface chemistry variations among a series of laboratory-produced biochars, Geoderma 163 (3) (2011) 247–255.
[46] A.B.D. Nandiyanto, R. Oktiani, R. Ragadhita, How to read and interpret FTIR spectroscope of organic material, Indonesian J. Sci. Technol. 4 (1) (2019) 97–118.
[47] A. Munajad, C. Subroto, Fourier transform infrared (FTIR) spectroscopy analysis of transformer paper in mineral oil-paper composite insulation under accelerated thermal aging, Energies 11 (2) (2018) 364.
[48] O. Üner, Ü. Geçgel, Y. Bayrak, Adsorption of methylene blue by an efficient activated carbon prepared from citrullus lanatus rind: kinetic, isotherm, thermodynamic, and mechanism analysis, Water Air Soil Pollut. 227 (7) (2016) 247.
[49] Z. Hao, et al., Magnetic particles modification of coconut shell-derived activated carbon and biochar for effective removal of phenol from water, Chemosphere 211 (2018) 962–969.
[50] A.A.H. Saeed, et al., Pristine and magnetic kenaf fiber biochar for Cd2+ adsorption from aqueous solution, Int. J. Environ. Res. Public Health 18 (15) (2021) 7949.
[51] I. Ali, et al., Encapsulated green magnetic nanoparticles for the removal of toxic Pb2+ and Cd2+ from water: development, characterization and application, J. Environ. Manage. 234 (2019) 273–289.
[52] A.H. Jawad, et al., Adsorption and mechanism study for methylene blue dye removal with carbonized watermelon (Citrullus lanatus) rind prepared via one-step liquid phase H2SO4 activation, Surfaces and Interfaces 16 (2019) 76–84.
[53] P. Barpanda, G. Fanchini, G.G. Amatucci, Structure, surface morphology and electrochemical properties of brominated activated carbons, Carbon 49 (7) (2011) 2538–2548.
[54] Chen, W., et al., Effect of Temperature on the Evolution of Physical Structure and Chemical Properties of Bio-char, Derived from Co-pyrolysis of Lignin with High-Density Polyethylene. 2016, 2016. 11(2): p. 14.
[55] P. Zhang, et al., A green biochar/iron oxide composite for methylene blue removal, J. Hazard. Mater. 384 (2020), 121286.
[56] K. Zhong, et al., Nitrogen-doped biochar derived from watermelon rind as oxygen reduction catalyst in air cathode microbial fuel cells, Appl. Energy 242 (2019) 516–525.
[57] P.B. Kharat, et al., Exploration of thermoacoustics behavior of water based nickel ferrite nanofluids by ultrasonic velocity method, J. Mater. Sci. Mater. Electron. 30 (7) (2019) 6564–6574.
[58] C. Yu, et al., Removal of Cu(ii) from aqueous solution using Fe3O4–alginate modified biochar microspheres, RSC Advances, 7 (84) (2017) 53135–53144.
[59] C. Santhosh, et al., Synthesis and characterization of magnetic biochar adsorbents for the removal of Cr(VI) and Acid orange 7 dye from aqueous solution, Environ. Sci. Pollut. Res. 27 (26) (2020) 32874–32887.
[60] X. Liu, et al., High yield conversion of biowaste coffee grounds into hierarchical porous carbon for superior capacitive energy storage, Sci. Rep. 10 (1) (2020) 1–12.
[61] X. Cai, et al., Design and preparation of chitosan-crosslinked bismuth ferrite/biochar coupled magnetic material for methylene blue removal, Int. J. Environ. Res. Public Health 17 (1) (2020) 6.
[62] J. Yu, et al., One-pot synthesis of highly ordered nitrogen-containing mesoporous carbon with resorcinol–urea–formaldehyde resin for CO2 capture, Carbon 69 (2014) 502–514.
[63] F. Kapteijn, et al., The development of nitrogen functionality in model chars during gasification in CO2 and O2, Carbon 37 (7) (1999) 1143–1150.
[64] T. Wei, et al., A Facile and low-cost route to heteroatom doped porous carbon derived from broussonetia papyrifera bark with excellent supercapacitance and co2 capture performance, Sci. Rep. 6 (2016) 22646.
[65] Z. Li, et al., Mesoporous nitrogen-rich carbons derived from protein for ultra-high capacity battery anodes and supercapacitors, Energy Environ. Sci. 6 (3) (2013) 871–878.
[66] H. Li, et al., Biochar derived from watermelon rinds as regenerable adsorbent for efficient removal of thallium(I) from wastewater, Process Saf. Environ. Prot. (2019).
[67] Z. Wang, et al., The influence and mechanism of different acid treatment to activated carbon used as air-breathing cathode catalyst of microbial fuel cell, Electrochim. Acta 246 (2017) 830–840.
[68] M.A. Ahmad, N. Ahmad, O.S. Bello, Modified durian seed as adsorbent for the removal of methyl red dye from aqueous solutions, Appl. Water Sci. 5 (4) (2015) 407–423.

[69] J. Dong, S. Li, Y. Ding, Anchoring nickel-cobalt sulfide nanoparticles on carbon aerogel derived from waste watermelon rind for high-performance asymmetric supercapacitors, J. Alloys Compd. 845 (2020), 155701.
[70] K. Thines, et al., A new route of magnetic biochar based polyaniline composites for supercapacitor electrode materials, J. Anal. Appl. Pyrolysis 121 (2016) 240–257.
[71] K. Xie, et al., Synthesis and supercapacitor performance of polyaniline/nitrogen-doped ordered mesoporous carbon composites, Nanoscale Res. Lett. 13 (1) (2018) 163.
[72] Q. Li, et al., An amino-functionalized metal–organic framework nanosheet array as a battery-type electrode for an advanced supercapattery, Dalton Trans. 48 (46) (2019) 17163–17168.
[73] A. Muzaffar, et al., A review on recent advances in hybrid supercapacitors: Design, fabrication and applications, Renew. Sustain. Energy Rev. 101 (2019) 123–145.
[74] N. Duraisamy, et al., Development of asymmetric device using Co3(PO4)2 as a positive electrode for energy storage application, J. Mater. Sci. Mater. Electron. 30 (8) (2019) 7435–7446.
[75] C. Dong, et al., Advances in cathode materials for high-performance lithium-sulfur batteries, iScience 6 (2018) 151–198.
[76] M. Cui, X. Meng, Overview of transition metal-based composite materials for supercapacitor electrodes, Nanoscale Adv. 2 (12) (2020) 5516–5528.
[77] M. Zhi, et al., Nanostructured carbon–metal oxide composite electrodes for supercapacitors: a review, Nanoscale 5 (1) (2013) 72–88.
[78] K. Ren, et al., Recent developments of transition metal compounds-carbon hybrid electrodes for high energy/power supercapacitors, Nano-Micro Letters 13 (1) (2021) 129.
[79] Z. Wang, et al., Synthesis of graphene–NiFe2O4 nanocomposites and their electrochemical capacitive behavior, J. Mater. Chem. A 1 (21) (2013) 6393–6399.
[80] A. Soam, et al., Synthesis of nickel ferrite nanoparticles supported on graphene nanosheets as composite electrodes for high performance supercapacitor, ChemistrySelect 4 (34) (2019) 9952–9958.
[81] W. Wang, et al., Ternary nitrogen-doped graphene/nickel ferrite/polyaniline nanocomposites for high-performance supercapacitors, J. Power Sources 269 (2014) 250–259.
[82] M.B. Askari, P. Salarizadeh, Binary nickel ferrite oxide (NiFe2O4) nanoparticles coated on reduced graphene oxide as stable and high-performance asymmetric supercapacitor electrode material, Int. J. Hydrogen Energy 45 (51) (2020) 27482–27491.
[83] T. Uzzaman, et al., Electrochemical performance of NiFe2O4 nanostructures incorporating activated carbon as an efficient electrode material, Ceram. Int. 47 (8) (2021) 10733–10741.
[84] B. Mordina, et al., Binder free high performance hybrid supercapacitor device based on nickel ferrite nanoparticles, J. Energy Storage 31 (2020), 101677.
[85] H. Pang, et al., Porous nickel oxide microflowers synthesized by calcination of coordination microflowers and their applications as glutathione electrochemical sensor and supercapacitors, Electrochim. Acta 85 (2012) 256–262.
[86] E. Frackowiak, F. Béguin, Carbon materials for the electrochemical storage of energy in capacitors, Carbon 39 (6) (2001) 937–950.
[87] A. Numan, et al., Facile sonochemical synthesis of 2D porous Co3O4 nanoflake for supercapattery, J. Alloys Compd. 819 (2020), 153019.
[88] P. Wang, et al., Ammonium vanadium oxide framework with stable NH4+ aqueous storage for flexible quasi-solid-state supercapacitor, Chem. Eng. J. 427 (2022), 131548.
[89] Y. Zhang, et al., Alkali etching metal silicates derived from bamboo leaves with enhanced electrochemical properties for solid-state hybrid supercapacitors, Chem. Eng. J. 417 (2021), 127964.
[90] Y. Huang, et al., Sulfurized activated carbon for high energy density supercapacitors, J. Power Sources 252 (2014) 90–97.
[91] W. Xiong, et al., A novel synthesis of mesoporous carbon microspheres for supercapacitor electrodes, J. Power Sources 196 (23) (2011) 10461–10464.
[92] J. Zhang, J. Jiang, X.S. Zhao, Synthesis and capacitive properties of manganese oxide nanosheets dispersed on functionalized graphene sheets, J. Phys. Chem. C 115 (14) (2011) 6448–6454.
[93] J. Iqbal, et al., Ternary nanocomposite of cobalt oxide nanograins and silver nanoparticles grown on reduced graphene oxide conducting platform for high-performance supercapattery electrode material, J. Alloys Compd. 821 (2020), 153452.
[94] M.Z. Iqbal, et al., Strontium phosphide-polyaniline composites for high performance supercapattery devices, Ceram. Int. 46 (8) (2020) 10203–10214.
[95] L. Guan, L. Yu, G.Z. Chen, Capacitive and non-capacitive faradaic charge storage, Electrochim. Acta 206 (2016) 464–478.
[96] L. Yu, G.Z. Chen, Supercapatteries as high-performance electrochemical energy storage devices, Electrochem. Energy Rev. 3 (2) (2020) 271–285.
[97] M. Genovese, et al., High capacitive performance of exfoliated biochar nanosheets from biomass waste corn cob, J. Mater. Chem. A 3 (6) (2015) 2903–2913.
[98] X. Dong, et al., Ammonia-etching-assisted nanotailoring of manganese silicate boosts faradaic capacity for high-performance hybrid supercapacitors, Sustain. Energy & Fuels 4 (5) (2020) 2220–2228.
[99] X. Wang, et al., Fabrication of vanadium sulfide (VS4) wrapped with carbonaceous materials as an enhanced electrode for symmetric supercapacitors, J. Colloid Interface Sci. 574 (2020) 312–323.
[100] S. Yang, et al., Biomass derived interconnected hierarchical micro-meso-macro-porous carbon with ultrahigh capacitance for supercapacitors, Carbon 147 (2019) 540–549.
[101] N.R. Chodankar, et al., An innovative concept of use of redox-active electrolyte in asymmetric capacitor based on MWCNTs/MnO_2 and Fe_2O_3 thin films, Sci. Rep. 6 (1) (2016) 1–14.
[102] M. Nangir, A. Massoudi, S.A. Tayebifard, Investigation of the lithium-ion depletion in the silicon-silicon carbide anode/electrolyte interface in lithium-ion battery via electrochemical impedance spectroscopy, J. Electroanal. Chem. 873 (2020), 114385.
[103] H.-J. Kim, et al., Well-dispersed NiS nanoparticles grown on a functionalized CoS nanosphere surface as a high performance counter electrode for quantum dot-sensitized solar cells, RSC advances, 6 (35) (2016) 29003–29019.
[104] K. Scott, Electrochemical principles and characterization of bioelectrochemical systems. Microbial Electrochemical and Fuel Cells, Elsevier, 2016, pp. 29–66.